# Cation-vacancy ordering in dehydrated Na 6 [ AlSiO 4 ] 6

Scott R. Shannon, Branton J. Campbell, Horia Metiu, and Nick P. Blake

Citation: The Journal of Chemical Physics **113**, 10215 (2000); doi: 10.1063/1.1319350
View online: http://dx.doi.org/10.1063/1.1319350
View Table of Contents: http://scitation.aip.org/content/aip/journal/jcp/113/22?ver=pdfcov
Published by the AIP Publishing

# Cation-vacancy ordering in dehydrated $Na_6[AlSiO_4]_6$

Scott R. Shannon
*Department of Chemistry, University of California, Santa Barbara, California 93106*

Branton J. Campbell
*Materials Research Laboratory, University of California, Santa Barbara, California 93106*

Horia Metiu
*Department of Chemistry and Department of Physics, University of California, Santa Barbara, California 93106*

Nick P. Blake
*Department of Chemistry, University of California, Santa Barbara, California 93106*

(Received 30 June 2000; accepted 29 August 2000)

The low-temperature cation-ordered superstructure of anhydrous sodium sodalite, a zeolite with composition $Na_6[AlSiO_4]_6$, has been determined through the use of both density functional theory (DFT) and classical force-field lattice energy minimizations. The charge-balancing $Na^+$ cations are assumed to occupy their characteristic locations within the cubic alumino–silicate framework near the centers of the 6-ring windows. Within the constraints of the volume-doubled pseudotetragonal supercell reported in a previous x-ray diffraction study [B. Campbell, S. R. Shannon, H. Metiu, and N. P. Blake (submitted)], all possible arrangements of cations and vacancies amongst the 6-ring window sites were considered. Force-field calculations employing the *ab initio* based potential energy function derived by Blake, Weakliem, and Metiu [J. Phys. Chem. B **102**, 67 (1998)] and the empirical shell-model potential of Catlow *et al.* [J. Chem. Soc. Commun. **1984**, 1271; Mol. Simul. **1**, 207 (1988)], were used to perform full lattice-energy minimizations of each configuration, and to assess their relative stabilities both before and after minimization. The most stable configurations were then examined in more detail via *ab initio* density functional calculations in the generalized gradient approximation. The lowest-energy supercell ordering proved more stable than the lowest-energy parent cell ordering, and also yielded a pseudotetragonal distortion (space group $Pnc2$) and a calculated diffraction pattern that qualitatively match experimental results. The structural influences that contribute to the low energy of the correct vacancy ordering are described in detail. © *2000 American Institute of Physics.* [S0021-9606(00)00744-3]

## I. INTRODUCTION

The crystal structure of the mineral sodalite, $Na_8^+[AlSiO_4^-]_6Cl_2^-$ (NaCl–SOD), was first determined by Pauling.[1] It possesses a three-dimensional framework consisting of tetrahedrally-coordinated Al and Si (called T-atoms) bound to one another via O bridges. The framework is therefore a three-dimensional network of corner-sharing $SiO_4$ and $AlO_4$ tetrahedra. Loewenstein's rule of aluminum avoidance in alumino–silicate frameworks states that Al–O–Al linkages are highly unfavorable, which results in a natural lower limit of 1 on the molar Si/Al ratio. Sodalite realizes this limit and must therefore have an ordered Si/Al distribution in order to avoid the unfavorable linkages, in contrast to the Al disorder common to more siliceous zeolites. Because the Al–O and Si–O bond lengths are significantly different (1.74 Å vs 1.61 Å, respectively) it is possible to distinguish the Al and Si sites using structural parameters obtained from x-ray diffraction.

The sodalite framework can be conveniently described in terms of the sodalite cage, also called the $\beta$-cage, several representations of which are shown in Fig. 1. Adjacent sodalite cages are connected to one another by sharing common 4-ring or 6-ring faces,[2] resulting in a body-centered cubic lattice of cages as shown in Fig. 2 (the unit cell contains two $\beta$-cage volumes). A pure $SiO_2$ framework would be charge neutral, however the presence of trivalent Al at some of the tetrahedral sites requires a negatively charged framework to ensure filled valence bands. In NaCl–SOD, extra-framework $Na^+$ and $Cl^-$ ions are present to balance this negative charge. Each $Na^+$ ion occupies a site near the center of one of the $\beta$-cage 6-rings at a position located along the line that extends from one cage center to another through the center of the 6-ring window. NaCl–SOD (Ref. 2) has four $Na^+$ ions per cage located at the vertices of a tetrahedron such that each 6-ring window has one associated $Na^+$ cation. Despite the fact that four $Na^+$ ions overcompensate for the three framework Al atoms per cage, it is energetically favorable to coordinate a cation to every 6-ring window. Charge neutrality is achieved by the additional inclusion of a $Cl^-$ ion at the center of each cage.[2] The maximum topological symmetry of the sodalite framework is $Im\bar{3}m$, but the differentiation of Al and Si sites, together with the well-known ''partial-collapse'' distortion identified by Pauling, combine to reduce the actual symmetry of NaCl–SOD to $P\bar{4}3n$ ($T_d^4$).

A variety of extra-framework cations and anions can be substituted for $Na^+$ (e.g., $Na^+$, $K^+$ or $Ag^+$) or $Cl^-$ (e.g.,

 

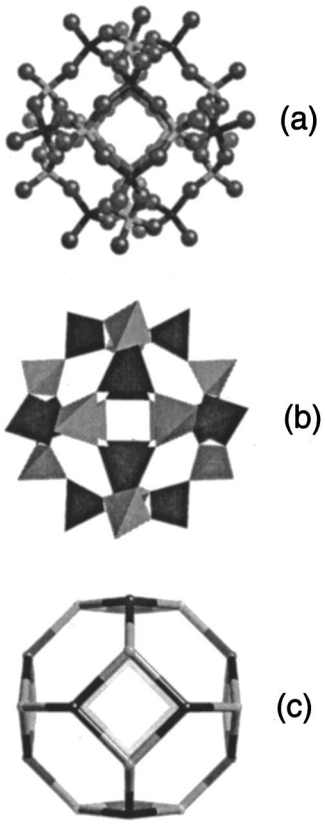


FIG. 1. The structure of the sodalite cage. (a) All atoms explicitly shown: O atoms are two coordinated and Si and Al are four coordinated. (b) Represented as a network of vertex-sharing $SiO_4$ and $AlO_4$ are shown as tetrahedra, (vertices corresponding to O atoms). (c) Stick view: nodes correspond to Si and Al, while sticks represent bridging oxygens.

$SO_4^{2-}$ or $OH^-$).[3] Charge balance can also be accomplished by omitting the cage-center $Cl^-$ ion and the excess $Na^+$ ion in each cage, anhydrous sodium sodalite $Na_6^+[AlSiO_4^-]_6$ ($Na_6$–SOD) being one such example. $Na_6$–SOD has only six $Na^+$ cations with which to occupy the eight 6-ring window sites per unit cell, leaving two sites vacant. The possibility then exists for a low-temperature cation-vacancy ordering.

The first study of the structure of $Na_6$–SOD was published by Felsche, Luger, and Baerlocher.[4] They refined the structure against laboratory powder x-ray diffraction (PXD) data collected at 675 K using cubic space group $P\bar{4}3n$ and a cation-disorder model in which each 6-ring window site was 75% occupied. Sieger[5] reported that $Na_6$–SOD undergoes a phase transition near 500 K, evidence for which was the onset of a series of PXD superlattice peaks below the transition temperature that could not be indexed. From Bragg peak splittings and superlattice peaks in variable temperature synchrotron PXD measurements, Campbell *et al.*[6] report that this transition includes the cooperative formation of a volume-doubled pseudotetragonal supercell and a one-dimensional long-period modulation. They suggest that the commensurate supercell, related to the original cubic cell by a 45° rotation about a fourfold axis, is associated with the ordering of vacant cation sites, and that the long-period modulation involves deviations of the $TO_4$ tetrahedra from their average orientations. They further find that the high-temperature cation-disordered phase is best described by a dynamic-tilt model (cubic space group $Pm\bar{3}n$) in which the framework tetrahedra fluctuate locally between opposite ''partial collapse'' angles, as was the case for high-temperature $Ag_6[AlSiO_4]_6$ ($Ag_6$–SOD).[7]

A detailed structural model of this low-temperature cation-vacancy-ordered phase is desired. But whereas single-crystal x-ray diffraction is ordinarily the means of such a structure determination, anhydrous $Na_6$–SOD can only be obtained as a microcrystalline powder. Hydrothermal synthesis results in a hydrated product. Subsequent dehydration results in a significant volume change that extensively fractures any suitable crystals. While PXD data has been used to determine the pseudotetragonal (orthorhombic) supercell parameters,[6] it proved insufficient for identifying a specific cation-vacancy ordering without further supporting information. Campbell *et al.*[6] enumerated all possible cation-vacancy orderings on the primitive cubic lattice of 6-ring window sites in $Na_6$–SOD within the constraints of the observed pseudotetragonal supercell. There are 3 such unique configurations for the original cubic unit cell (the 42 atom cell) and 88 unique configurations for the supercell (the 84 atom cell). In this paper each of these configurations is studied to see which are energetically favored. Initially each configuration is minimized using force-field techniques. Those of lowest energy are then studied using density functional theory. These structures are then compared with existing experimental PXD data. In understanding the factors that govern favorable vacancy orderings we show why the pseudotetragonal supercell is preferred over the smaller parent cell.

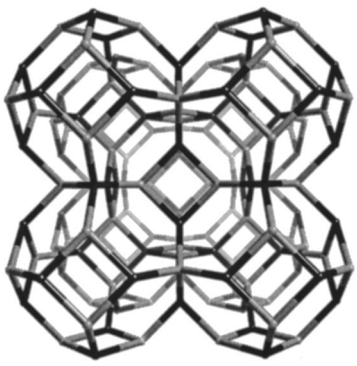

FIG. 2. The sodalite framework. Note how the $\beta$ cage of Fig. 1 is used to construct a body-centered cubic lattice of cages.

## II. THE METHOD OF COMPUTATION

In the DFT calculations presented here, all valence electrons are explicitly considered and the effect of the core electrons is included as an ultrasoft pseudopotential. This pseudopotential was generated according to the scheme outlined by Rappe, Rabe, Kaxiras, and Joannopoulos.[8] Cutoff radii were $r_s = r_p = r_d = 2.48$ bohr for Si, $r_s = r_p = r_d = 2.65$ bohr for Al, and $r_s = r_p = 3.61$, $r_d = 2.70$ bohr for Na. For oxygen, both ''soft'' and ''hard'' ultrasoft potentials were tried. The soft potential used $r_s = 1.52$ bohr and $r_p = 1.90$ bohr, while the hard potential used $r_s = 1.40$ and $r_p = r_d = 1.55$ bohr. The Kohn–Sham equation was solved by using a plane-wave ba-

sis set. Exchange and correlation effects are accounted for using the generalized gradient approximation (GGA) as outlined by Perdew and Wang.[9]

All DFT calculations use the Vienna *Ab initio* Simulation Package (VASP) of Kresse, Fürthmuller, and Hafner.[10,11] The chosen plane wave cut-off was 396 eV for the ''hard'' ultrasoft pseudopotential, which was used for all calculations except where explicitly stated otherwise, and 270 eV for the ''soft'' ultrasoft pseudopotential. Owing to the prohibitive size of the cell, *k*-point sampling was restricted to the $\Gamma$ point (see below for a test of this approximation). This, and the fact we are dealing with insulating systems, allows for the use of a simple Gaussian smearing of the Fermi distribution, with a value of $kT=0.2\,\mathrm{eV}$, to simulate a finite temperature and thus aid convergence. A complete minimization of the ionic positions, cell shape, and cell volume was performed—the RMM-DIIS method was used for electronic minimization, while a conjugate gradient technique was employed for ionic minimization. Changes in cell volume and shape are determined via a calculation of the stress tensor. The electronic charge density for the 84-atom supercell was stored in a $180\times180\times126$ point grid. An energy difference of $10^{-4}$ eV was used for the iterative cut-off for electronic convergence while a difference of $10^{-3}$ eV was used for ionic convergence.

As we are mainly interested in energy *differences* between various ionic configurations, we expect that any associated systematic errors will cancel, leading to meaningful results for the various energy orderings. To estimate the absolute errors in our calculated unit cell basis vectors we have calculated the derivatives $\partial^2 E^{\mathrm{tot}}/\partial \mathbf{L}^2$, where $E^{\mathrm{tot}}$ is the total cell energy per unit volume and $\mathbf{L}$ the cells basis vectors, using finite differences. If we assume that the cell energy varies harmonically for small variations in the basis vectors about the minimum, we can estimate the implied error $\delta L$ in $\mathbf{L}$ for the convergence criterion chosen in these calculations. In this way we estimate that the errors in the calculated parameters for the 84 atom unit cells are $|a,b|=\pm0.019$ Å, $|c|=\pm0.014$ Å, $|\alpha,\beta|=\pm0.15°$, $|\gamma|=\pm0.18°$. Those for the 42 atom unit cells are given by the errors in $|c|$ and $|\alpha,\beta|$.

In order to assess the accuracy of these density functional calculations and compare the predictive capabilities of both the local density approximation (LDA) and the GGA, we have used the structure of NaCl–SOD as a test case. This material has been rigorously characterized by x-ray diffraction. There is no ambiguity regarding the location of the $Na^+$ cations which arrange themselves in a tetrahedron within each cage with a $Cl^-$ anion at the center while still coordinating to the oxygens of their respective 6-ring windows. The results for NaCl–SOD are shown in Table I for both the LDA and the GGA calculations.

The LDA appears to consistently underestimate the Si–O and Al–O bond lengths by roughly 0.5% while GGA overestimates them by about 0.7%. However GGA does better for Si–O–Al bond angles and framework ''partial collapse'' angles. As a consequence the GGA lattice constants are only 0.5% larger than experiment, while LDA underestimates the cell edge by 1.5%. In order to evaluate the effect of increasing the number of *k*-points over which the density is sampled, we have also performed the calculation for NaCl–SOD using 4 *k*-points instead of 1. This led to a reduction in the total energy by 0.06 eV and a change of 0.003 Å in the cell edge. The success of these calculations show that they have considerable predictive power.

TABLE I. Bond lengths, angles, and partial collapsing angles $\phi$ for NaCl–SOD. Standard deviations are shown in parentheses. Experimental results are from Hassan and Grundy (Ref. 2).

| | NaCl–SOD | | |
|---|---|---|---|
| | GGA | Experiment | LDA |
| L(Å) | 8.925 | 8.880 | 8.746 |
| Si–O–Al | 137.45(0.32) | 138.2 | 135.25(0.19) |
| O–Si–O | 109.49(2.52) | 109.47 | 109.49(2.45) |
| O–Al–O | 109.47(1.15) | 109.46 | 109.47(1.07) |
| Si–O (Å) | 1.632(0.001) | 1.62 | 1.614(0.00) |
| Al–O (Å) | 1.753(0.000) | 1.74 | 1.730(0.00) |
| Na–O (Å) (1) | 2.362(0.002) | 2.352 | 2.272(0.001) |
| Na–O (Å) (2) | 3.115(0.021) | 3.086 | 3.092(0.008) |
| Na–Na (Å) | 4.489(0.010) | 4.466 | 4.370(0.05) |
| O–O (Si) (Å) | 2.666(0.041) | 2.65 | 2.636(0.039) |
| O–O (Al) (Å) | 2.862(0.020) | 2.84 | 2.824(0.019) |
| $\phi$ (Si) | 24.50(0.083) | 23.9 | 26.25(0.050) |
| $\phi$ (Al) | 22.99(0.15) | 22.4 | 24.68(0.081) |

Because the density functional calculations for such a large system are computationally expensive for a unit cell as large as that of sodalite, preliminary calculations were carried out using a classical force-field approach with two *different* potentials. The first potential used was very similar to that proposed by Blake, Weakliem, and Metiu[12] but the three-body term has been simplified to make it compatible with the General Lattice Utility Program (GULP) of Gale.[13] The modified form, see Table II(a), is

$$\Phi_{ij}=\frac{q_i q_j}{r_{ij}}+A_{ij}e^{-r_{ij}/\rho_{ij}}-\frac{C_{ij}}{r_{ij}^6}+\frac{1}{2}\sum_{n=1}^{N}\left(k_{ijn}[\vartheta_{ijn}-\vartheta_{ijn}^0]^2\right). \quad (1)$$

Here $\Phi_{ij}$ is the interaction energy between atoms *i* and *j*. The first term represents the long-range electrostatic interactions between the effective partial charges of the two nuclei, separated by a distance $r_{ij}$. The second and third terms are a Buckingham potential, which represents the bonding and the nonbonding interactions between the two atoms. The last term approximates the 3-body O–T–O (T=Si, Al) and Al–O–Si bending.

The values of the parameters in Eq. (1) were fitted so as to reproduce MP2 *ab initio* data, as well as the structures, elastic constants and vibrational spectra of selected sodalites. The O–T–O terms chosen reproduce the original potential at the equilibrium bond lengths for Si–O and Al-O (in the original potential bond-stretching and bending were coupled). The Si–O–Al bending term replaces the Al–Si pair potential in the original potential and is strictly a nearest neighbor interaction. As with the earlier work the Si–O–Al bending term was chosen to reproduce the symmetric–

TABLE II. (a) Parameters for the BWM potential as described by Eq. (1). (b) Parameters for the shell model potential as described by Eq. (1) and Catlow *et al.* (Refs. 15 and 16).

| (a) | (eV deg$^{-2}$) | $R_{cut}(1)$ (Å) | $R_{cut}(1)$ (Å) | $R_{cut}(3)$ (Å) | $\theta$ (deg) | |
|---|---|---|---|---|---|---|
| | O–Si–O | −0.66 | 1.80 | 1.80 | 3.50 | 109.47 |
| | O–Al–O | −0.66 | 1.90 | 1.90 | 3.50 | 109.47 |
| | Si–O–Al | 1.80 | 1.90 | 1.90 | 4.50 | 159.00 |
| | 2-body | $A$ (eV) | $C$ (eV Å$^6$) | $\rho$ (Å) | $R_{cut}$ (Å) | $Q(e)$ |
| | Si–O | 27 374.0 | 145.527 | 0.191 714 | 12.0 | Si=1.6 |
| | Al–O | 28 643.2 | 255.361 | 0.206 597 | 12.0 | Al=0.6 |
| | Na–O | 2 787.05 | 39.793 | 0.267 260 | 12.0 | O=−0.8 |
| | O–O | 2 727.11 | 119.000 | 0.317 500 | 12.0 | Na=1.0 |
| (b) | 3-body | $k$ (eV deg$^{-2}$) | $R_{cut}(1)$ (Å) | $R_{cut}(1)$ (Å) | $R_{cut}(3)$ (Å) | $\theta$ (deg) |
| | O($c$)–Si–O($s$) | 2.097 24 | 1.90 | 1.90 | 3.50 | 109.47 |
| | O($c$)–Al–O($s$) | 2.097 24 | 1.90 | 1.90 | 3.50 | 109.47 |
| | 2-body | $A$ (eV) | $C$ (eV Å$^6$) | $\rho$ (Å) | $R_{cut}$ (Å) | $Q(e)$ |
| | Si($c$)–O($s$) | 1283.91 | 10.661 58 | 0.320 520 | 12.0 | Si=4.0 |
| | Al($c$)–O($s$) | 1460.30 | 0.000 000 | 0.299 120 | 12.0 | Al=3.0 |
| | O($s$)–O($s$) | 22764.0 | 27.880 00 | 0.149 000 | 12.0 | Na=1.0 |
| | Na($c$)–O($s$) | 1226.84 | 0.000 000 | 0.306 500 | 12.0 | |
| | Core-shell | $k$ (eV Å$^{-2}$) | | | | O($s$)=−2.869 02 |
| | O($c$)–($s$) | 74.92 | | | | O($c$)=0.869 02 |

asymmetric framework frequencies seen in the infrared absorption. The remaining details of the fitting are as in the work of Blake *et al.*[12]

The second type of classical potential used is based on the shell model developed originally by Dick and Overhauser[14] [see Table II(b)]. The potential used here is a shell model for the aluminosilicates derived by Catlow and co-workers,[15,16] and is an empirical potential designed for silicates and aluminosilicates. The shell model allows for the O in the structure to be polarizable, by connecting the inner core (the charge of which is a fitting parameter) to an electron shell of zero mass, by means of a harmonic spring (the force constant and the charge are fitted parameters). The final potential has a similar form to the BWM potential, with the addition of a Harmonic core-shell interaction. This potential is used here since it is normally considered one of the most accurate empirical alumino–silicate potentials.

In these calculations a complete minimization of both the cell parameters (i.e., constant pressure) and all the atomic positions were performed. Coulomb interactions were handled by an Ewald summation, while the minimizations were performed using a rational function optimization to ensure that the correct cell symmetry was obtained. No imaginary eigenvalues were obtained for the Hessian, indicating that true energy minima were reached.

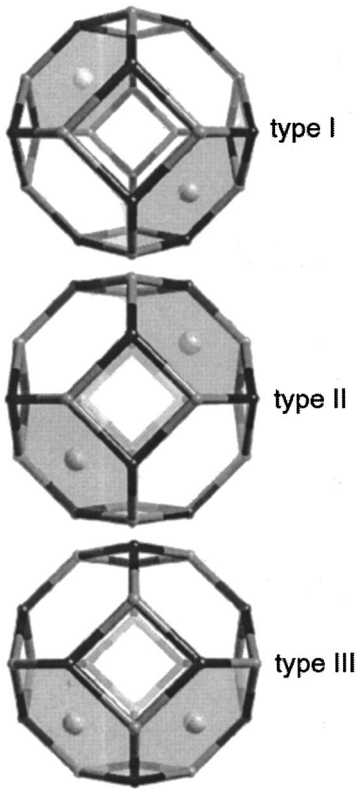


FIG. 3. The three types of vacancy distribution in the sodalite cage. Here the spheres represent the vacancies. A $Na^+$ ion is located at the center of any six-ring window that does not have a sphere at its center. The cage at the top corresponds to the type-I cage, the one in the middle is the type-II cage, and the bottom figure is the type-III cage.

## III. VACANCY ORDERINGS WITHIN THE ORIGINAL CUBIC 42-ATOM UNIT CELL

In the original 42-atom cell, the two cation vacancies can be distributed amongst the 8 available 6-ring window sites in

TABLE III. The calculated energies (per unit cell) of the type-II and type-III vacancy configurations relative to the energy of the type-I configuration. The first row contains the $Na^+$–$Na^+$ Coulomb energies of the unrelaxed solids in which the Na cations have been placed at the centers of their 6-ring windows. The last three rows contain total minimized structural energies obtained using GGA DFT, the classical potential of Blake, Weakliem, and Metiu (Ref. 12), and the classical shell-model potential of Catlow and coworkers (Refs. 15 and 16), respectively.

| | $E_{III}-E_I$ (eV) | $E_{II}-E_I$ (eV) |
|---|---|---|
| $Na^+$–$Na^+$ | 1.115 | 0.347 |
| GGA | 0.154 | 0.080 |
| BWM | 0.595 | 0.241 |
| shell | 0.365 | 0.155 |

(8!)/(6!2!)=28 different ways, the three unique (i.e., symmetry independent) arrangements being illustrated in Fig. 3. The *vacant* windows in each case are indicated by shading and by a sphere at the empty cation site. The filled cation sites are located very close to the centers of the 6-ring windows, though deviations from the window centers will be discussed in a later section. One might argue for placing two cations on opposite sides of the same window, but such configurations are easily discounted on the basis of their very high energies and need not be considered further. The three configurations in Fig. 3 can be evaluated according to the relative proximity of the two vacancies within the sodalite cage. The configuration for which the distance between vacancies is maximized shall be called ''type-I''—the two vacancies are located on a line in the [1 1 1] direction (i.e., a threefold symmetry axis). If the eight cation sites are viewed as forming the corners of a cube then the type I configuration places the vacancies opposite one another along a body diagonal of this cube. The type II configuration separates the two vacancies by placing them on a line in the [1 1 0] direction (along a face diagonal of the same cube), and the type III configuration separates two vacancies by placing them on a line in the [1 0 0] direction (nearest neighbors along a cube edge).

Table III contains the energy differences, $E_{III}-E_I$ and $E_{II}-E_I$, arising from four different sets of calculations on the three cation-vacancy arrangements. The first row of the table is the unminimized Coulomb repulsion energy associated with the $Na^+$ cation in their ideal positions at the 6-ring window centers, with no contribution from the framework. This energy clearly decreases as the average cation separation increases, so that the type-I configuration is most favored, while the type-III configuration, which has nearest-neighbor vacancies, has the highest energy. The other three rows are the results of structural energy minimizations that include the response of the framework to the vacancy ordering. These calculations reveal that type-III is still highly disfavored, while type-II has become comparable to type-I in energy.

TABLE IV. The unit cell geometries obtained from the GGA-DFT structural energy minimizations of the type I–II–III configurations. The length on the unit cell basis vectors are given by $|a|$, $|b|$, and $|c|$, while $\alpha$, $\beta$, and $\gamma$ are the angles between the vectors **b** and **c**, **a** and **c**, **a** and **b**, respectively. Errors are as calculated in the Computational Method.

| | $\lvert a\rvert$ (Å) | $\lvert b\rvert$ (Å) | $\lvert c\rvert$ (Å) | $\alpha$ | $\beta$ | $\gamma$ |
|---|---|---|---|---|---|---|
| I | 9.149 | 9.149 | 9.149 | 89.67 | 89.67 | 89.67 |
| II | 9.175 | 9.176 | 9.158 | 89.98 | 90.05 | 89.67 |
| III | 9.184 | 9.148 | 9.143 | 90.03 | 90.03 | 90.06 |

TABLE V. Bond lengths, bond angles, and partial collapsing angles for the three unique vacancy orderings of the 42-atom cell. Calculated by minimizing the GGA-DFT energy. Standard deviations are shown in parentheses.

| | I | II | III |
|---|---|---|---|
| Si–O–Al | 146.56(2.98) | 147.61(4.64) | 147.47(6.24) |
| O–Si–O | 109.48(3.57) | 109.48(3.89) | 109.46(3.69) |
| O–Al–O | 109.42(3.95) | 109.43(3.80) | 109.36(4.25) |
| Si–O (Å) | 1.629(0.013) | 1.629(0.013) | 1.629(0.016) |
| Al–O (Å) | 1.749(0.015) | 1.748(0.018) | 1.750(0.023) |
| Na–O (Å) (1) | 2.322(0.000) | 2.326(0.025) | 2.315(0.026) |
| Na–O (Å) (2) | 2.917(0.065) | 2.911(0.073) | 2.921(0.111) |
| Na–Na (Å) | 4.607(0.002) | 4.573(0.025) | 4.548(0.047) |
| O–O (Si) (Å) | 2.659(0.055) | 2.659(0.061) | 2.659(0.054) |
| O–O (Al) (Å) | 2.854(0.064) | 2.852(0.060) | 2.853(0.061) |
| $\phi$(Si) | 16.17(1.95) | 15.19(1.76) | 15.43(1.12) |
| $\phi$(Al) | 15.20(1.69) | 14.30(1.81) | 14.54(1.75) |

Table IV contains the cell geometries and Table V contains key structural parameters obtained from the GGA DFT calculations performed on the vacancy configurations in the 42-atom cell. The unit cell parameters from these calculations show closer agreement with experiment than previous DFT calculations on similar systems.[17,18] The average unit cell lengths calculated from Table IV, which range from 9.15 Å to 9.17 Å, are very similar to the experimental values of Campbell *et al.*,[6] which range from 9.07 Å at 100 K to 9.16 Å at 675 K. The generalized gradient correction is clearly important if one is interested in determining accurate Al–O–Si bond angles. The type-I, type-II, and type-III configurations drive slight rhombohedral, monoclinic, and orthorhombic distortions, respectively. Because the calculations employ no symmetry within the unit cell, some of the right angles in Table IV deviate slightly from 90° due to random errors within the limits of the accuracy of the calculations. These unit cell distortions are large enough to be experimentally distinguishable.

Each value in Table V is an average over the crystallographically distinct bonds or angles of the indicated type and configuration. The standard deviations from these average values are indicated in parentheses. While the framework distortions required to accommodate the different vacancy orderings lead to similar Si–O and Al–O bond lengths, they result in rather different Si–O–Al bond angles and partial collapse angles. The $SiO_4$ and $AlO_4$ tetrahedra are fairly rigid, but the bond angle about a shared oxygen vertex between two tetrahedra is quite flexible. A comparison of the three columns in Table V reveals the expected trend of increasing deviations from the average structure with decreasing structural symmetry. A lower symmetry means more internal degrees of freedom than can be activated in response to the vacancy ordering.

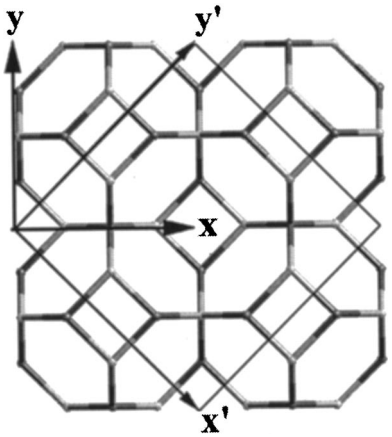


FIG. 4. The sodalite crystal, viewed along the [001] axis. The $x$ and $y$ coordinate axes correspond to the original cubic 42-atom unit cell, while the $x'$ and $y'$ coordinate axes correspond to the pseudo-tetragonal 84-atom supercell.

## IV. VACANCY ORDERINGS WITHIN THE PSEUDOTETRAGONAL 84-ATOM SUPERCELL

The type-I and type-II configurations yield similar structural energies when the framework response to the vacancy ordering is taken into account. Type-III, on the other hand, is discounted on the basis of its high-energy nearest-neighbor vacancies. Because the type-I and type-II configurations do not require a supercell description, they can also be discounted due to their inability to produce the diffraction superlattice peaks that have been reported[5,6] to arise below the ordering transition. They are, however, quite closely related to the pseudotetragonal (orthorhombic) supercell that was recently shown to form in the low-temperature phase.[6] This volume-doubled cell contains a total of 84 atoms and is related to the original cell by a 45° rotation in the $ab$ plane, as shown in Fig. 4, having lattice parameters approximately equal to $a \approx \sqrt{2}a_0$, $b \approx \sqrt{2}a_0$, $c \approx a_0$. The lattice vectors of the original cell (unprimed) and undistorted supercell (primed) are related by the transformation $\begin{bmatrix} x' \\ y' \end{bmatrix} = \begin{bmatrix} 1 & -1 \\ 1 & 1 \end{bmatrix} \begin{bmatrix} x \\ y \end{bmatrix}$.

The monoclinic unit cell distortion associated with the type-II configuration in Table IV is peculiar in that the $a$ and $b$ lattice parameters are essentially identical. Such a distortion is easily shown to be equivalent to a base-centered orthorhombic distortion in the supercell setting of Fig. 4. While the base-centering symmetry prevents the type-II vacancy ordering from producing superlattice peaks, there are other related vacancy orderings within the new supercell setting that can do so. Campbell *et al.*[6] enumerated each of the 88 unique arrangements of 4 vacancies among the 16 available sites in the supercell setting, and their scheme for labeling these configurations will be followed in the discussion below.

Beginning with each Na cation at the centers of its respective 6-ring window, classical force-field lattice energy minimizations were performed for each of these 88 cation-vacancy orderings using both the BWM and Shell model potentials. Since each starting configuration employs identical framework coordinates, the unminimized energy differences are purely a result of differences in $Na^+$–$Na^+$ repulsion energy. Figure 5 illustrates the unminimized energies from these configurations as well as the final minimized energies. Not only do the framework and unit cell distort in response to a given vacancy ordering, the Na cations shift slightly relative to their window sites to find the optimal overall arrangement. It is interesting to note that the relative energy rankings before and after minimization are quite similar, indicating that the gross differences associated with the starting $Na^+$–$Na^+$ Coulomb repulsion energies still define the trend after minimization. Minimization was, however, observed to interchange the relative energy rankings of configurations that already had similar energies.

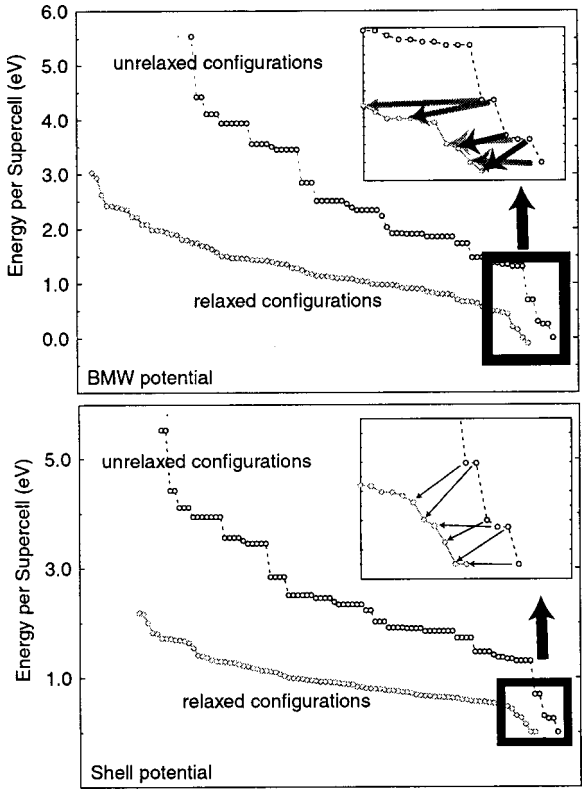


FIG. 5. Calculated lattice energies for the 88 unique cation orderings in the 84-atom supercell. The horizontal axis is meaningless and serves only to spread the data points out for visual clarity, from the highest energy at the far-left to the lowest energy at the far-right. In both graphs the upper curve corresponds to the initial unminimized lattice energies, and the lower curve the fully minimized lattice energies. Each initial configuration has the same set of framework atom coordinates, and the Na cations begin at the centers of their respective 6-ring windows. The upper graph is the result for the BMW potential and the lower graph for the shell model potential. The insets show the regions in the rectangles, while the arrows show how the orderings before and after relaxation relate to one another. In some instances minimization of one configuration resulted in the formation of another configuration.

Five of the six lowest-energy configurations, labeled #1, #5, #15, #24, #29 in Fig. 6, form a family of closely related vacancy orderings. Each consists of a series of parallel (110) planes of cation sites. These planes alternate with every other plane containing no vacancies at all, and those in between with 50% of the total ionic sites vacant. The five unique ways of arranging the vacancies in the half-vacant planes (within the supercell) ensure the avoidance of nearest-neighbor vacancies. Configurations #15 and #1 are actually

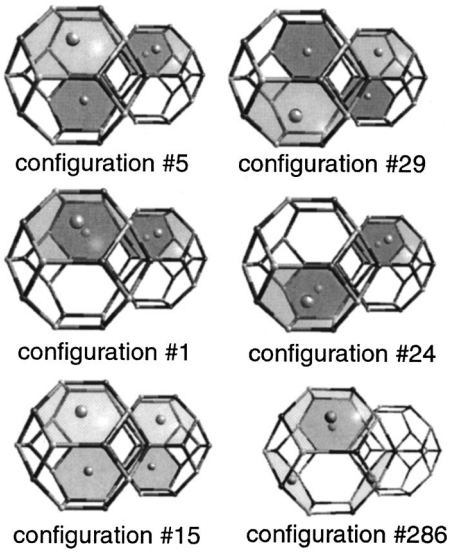


FIG. 6. The six lowest-energy vacancy configurations of the 84-atom supercell. This supercell contains 16 possible Na sites among which are 12 Na cations and 4 vacancies. The locations of the vacancies in each configuration are viewed here along the [1 0 0] axis of the supercell, with the [0 0 1] axis along the vertical direction. The vacancies are indicated by spheres, and the hexagonal windows in which they reside are shaded.

base-centered descriptions of the same type-I and type-II vacancy orderings of the 42-atom cubic cell. Configurations #5, #24, and #29 however, are primitive in the supercell setting. Configurations #29 and #24 contain only type-I cages and type-II cages, respectively, but differ from #15 and #1 in that the vacancy arrangements in neighboring cages are related by a $\frac{1}{2}[110]$ mirror glide perpendicular to [0 0 1] (supercell setting) that cuts through the cage centers. In fact, the Na cation lattices of #24 and #29 are identical if the sodalite framework is ignored, but differ in their orientations relative to the framework. Configuration #5 contains a mixture of 50% type-I and 50% type-II cages. Within this packing scheme of alternating [110] planes of vacancies and no vacancies the individual cages contain either type-I or type-II cages or both. In this way we see a relationship to the smaller parent cell paradigm where each ''cage'' may possess two vacancies. However, there is one other way of avoiding nearest neighbor vacancies that does not possess two vacancies per cage. This corresponds to #286 which puts all four vacancies in a tetrahedral arrangement in the same cage (see Fig. 6). Configuration #286 is unusual in that it contains one cage that has no vacancies while the neighboring cage has four tetrahedrally arranged vacancies. This results in structural properties somewhat different to the other five configurations.

As discussed above, taking into account the structural distortion caused by the vacancy ordering significantly narrows the energy gap between the type-I and type-II configurations in the 42-atom cell, though type-I still retains its position as the lowest-energy configuration. This effect is more pronounced in the 84-atom supercell with its larger number of degrees of freedom. This is seen in Table VI. Configuration #15 is the type-I vacancy ordering in the 84-atom supercell setting, and again has the lowest $Na^+$–$Na^+$ Coulomb repulsion energy prior to minimization. After minimization, however, when the structural response to the vacancy ordering has been taken into account, it is configuration #24 and not #15 that arises as the lowest energy arrangement. This is illustrated in the last three columns of Table VI which contain the results of the force-field calculations employing the BWM potential as well as well as more accurate *ab initio* GGA DFT calculations employing both the ''hard'' and ''soft'' ultrasoft oxygen pseudo-potentials. While the simple shell model potential (column 2) finds configuration #15 to essentially equivalent to that of #24, the more accurate and computationally intensive methods show that #24 is significantly more stable. Configuration #286 is exceptional in having a much greater initial $Na^+$–$Na^+$ repulsion energy while still relaxing to a structure having an energy comparable to the others.

TABLE VI. The energy of the 6 lowest energy configurations in eV per unit cell for the supercell relative to the energy of configuration #15. The configuration is given in the first column, the $Na^+$–$Na^+$ repulsion energy is in the second column, the third and fourth columns gives the minimum energies calculated with the shell model and the BWM force field (using GULP) while the last two columns show the minimum GGA energy (calculated with VASP) using soft and hard O pseudopotentials. The energy of configuration #15 is taken to be zero. The errors are as calculated in the Computational Method.

| Vacancy Config. | $Na^+$–$Na^+$ eV/uc | Shell eV/uc | BWM eV/uc | GGA(soft O) eV/uc | GGA(hard O) eV/uc |
|---|---|---|---|---|---|
| #1 (type-II) | 0.69 | 0.30 | 0.48 | 0.17 | 0.18 |
| #29 | 0.25 | 0.26 | 0.26 | 0.19 | 0.18 |
| #286 | 1.92 | 0.57 | 0.05 | 0.11 | 0.11 |
| #5 | 0.30 | 0.15 | 0.22 | 0.08 | 0.08 |
| #15 (type-I) | 0.00 | 0.00 | 0.00 | 0.00 | 0.00 |
| #24 | 0.25 | 0.00 | −0.04 | −0.04 | −0.03 |

Table VII contains the unit cell parameters that resulted from the DFT calculations on each of the six lowest-energy configurations. The orthorhombic cell of #1 is equivalent to a monoclinic cell with $a=b=9.148$ Å, $c=9.136$ Å, and $\gamma=89.59°$ in the parent cell setting, much as expected since configuration #1 is identical to the parent-cell type-II configuration. These values are only slightly smaller than those from the type-II simulation. The rhombohedral distortion of the type-I configuration is equivalent to a monoclinic distortion in the supercell setting, assuming special constraints on the monoclinic lattice parameters to maintain the proper number (2) of degrees of freedom. Although #15 is identical to the parent-cell type-I configuration, the monoclinic lattice

TABLE VII. Cell geometries obtained by minimizing the energy of the 84-atom configurations. All results reported are for the calculations performed with GGA. The errors are as calculated in the Computational Method.

| | $\lvert a\rvert$ (Å) | $\lvert b\rvert$ (Å) | $\lvert c\rvert$ (Å) | $\alpha$ | $\beta$ | $\gamma$ |
|---|---|---|---|---|---|---|
| #5 | 12.991 | 12.915 | 9.156 | 89.82 | 89.99 | 90.00 |
| #24 | 12.972 | 12.912 | 9.172 | 90.00 | 90.00 | 90.00 |
| #286 | 12.972 | 12.932 | 9.193 | 90.02 | 90.04 | 90.00 |
| #29 | 13.018 | 12.929 | 9.159 | 90.00 | 90.01 | 89.99 |
| #1 | 12.983 | 12.891 | 9.136 | 89.98 | 90.02 | 90.01 |
| #15 | 12.981 | 12.919 | 9.161 | 89.66 | 89.99 | 89.97 |

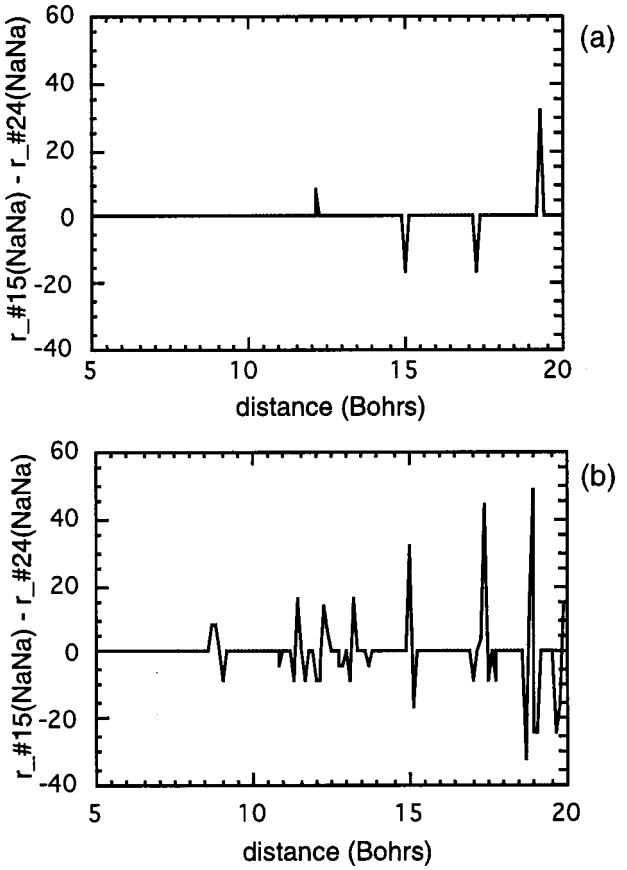


FIG. 7. Plots of the difference between the Na–Na pair correlation functions of configurations #15 and #24, $\rho_{15}^{\mathrm{NaNa}}(r)-\rho_{24}^{\mathrm{NaNa}}(r)$, using (a) the initial unminimized structures, and (b) the fully lattice energy minimized structures.

parameters of #15 violate those constraints, thus leading to a significantly nonrhombohedral distortion of the parent cell. In the simulation of configuration #15, the supercell setting affords new degrees of freedom to both framework and cations that were not available in the parent-cell simulation of the type-I configuration. The fact that the activation of these degrees of freedom does lower the overall structural energy offers a partial explanation of the fact that the experimentally observed supercell is not rhombohedral. Attention now turns to a more complete explanation.

In the supercell setting, configurations #24 and #29 drive primitive orthorhombic distortions with $Pnc2$ and $Pnn2$ symmetries, respectively, while configuration #5 drives a primitive monoclinic distortion with $P2$ symmetry. Of the available vacancy orderings, only #24 and #29 are consistent with the experimental diffraction data of Campbell *et al.*[6] in driving a primitive orthorhombic distortion and in yielding an acceptable set of systematically absent Bragg reflections. The systematic absences associated with the space-group symmetries of #24 and #29 might be used to experimentally distinguish between them also, in principle. But Campbell *et al.* report that their diffraction data are consistent with either structure. Configuration #24, however, unambiguously possesses the lowest overall structural energy, and clearly emerges as the best solution. From Figs. 3 and 6, it is clear that the vacancies in type-II cages lead to a local dipole moment oriented along (0 0 1). Because the dipole moments associated with the two cages of the type-II vacancy configuration (42-atom cell) are oppositely oriented, the resulting structure is antiferroelectric. Similarly, the arrangement of type-II cages in supercell configuration #24 leads to an antiferroelectric structure.

### A. The driving force for supercell formation

Why does a vacancy ordering (#24) requiring the formation of a supercell have a lower energy than the type-I ordering which is native to the original 42-atom cell? This result is surprising when considering that the rhombohedral type-I ordering minimized the $Na^+$–$Na^+$ repulsion energy prior to lattice energy minimization by a significant margin. This section will address this question. Figure 7(a) contains the difference between the Na–Na pair correlation functions of configurations #15 and #24, $\rho_{15}^{\mathrm{NaNa}}(r)-\rho_{24}^{\mathrm{NaNa}}(r)$, obtained using the unminimized structures in which the Na cations were located precisely at the centers of their respective 6-ring windows. All Na cations in configurations have an identical number of nearest neighbors, so that a difference arises only at Na–Na separation of 12 bohr—hence the similar energies. When the framework is allowed to relax, the lower symmetry of the orthorhombic system allows for some of the nearest neighbor Na cations to move away from one another. This is illustrated in Fig. 7(b) where differences in the Na–Na pair correlation function begin to register at around 8 bohr. As a result, #15 has closer nearest neighbors than #24 and more $Na^+$–$Na^+$ repulsion energy than #24.

Table VIII contains average bond lengths, bond angles, and Pauling ''partial collapse'' angles for each of the six lowest-energy configurations. As was the case in the 42-atom cell (see Table V), chemically reasonable bond lengths are preserved during the distortion, so that most of the structural change occurs in the bond angles of the flexible sodalite framework. Particularly notable in Table VIII is the large average Na–Na separation (4.663 Å) for configuration #24. Note, however, that among the remaining five structures, the average Na–Na separation does not appear to correlate well with the structural energy. Thus, while the $Na^+$–$Na^+$ repulsion energy is important, it is not the only factor.

Closer inspection reveals that configurations #15, #24, and #286 are unique in that no two vacant 6-ring windows share a common tetrahedral atom (Si or Al). This enhances the ability of the framework to stabilize the mutually repelling vacancies without overly compromising framework stability. From a structural standpoint relaxation manifests in a local decrease in the framework Pauling partial collapse angle. Since this corresponds to a change in the Si–O–Al angles only, the motion is facile in the structure and the energy cost is low. In Fig. 8 we show how a decrease in the partial collapse angle in #24 can help to increase the distance between vacancies. In #24 the vacancy pairs align along a translational axis of the solid and this makes it possible for all of the vacancy pairs to separate cooperatively, with the results that #24 is very stable. *This is the mechanism that drives the supercell formation*. It explains why the translational axes are $x'$ and $y'$ and not $x$ and $y$, since only when the framework distortion occurs along a symmetry axis can

TABLE VIII. Bond lengths, bond angles, and ''partial collapse'' angles ($\phi$) for the five lowest-energy vacancy configurations obtained from the *ab initio* GGA DFT calculations (averaged over the crystallographically unique bonds and angles). The quantities in parentheses are standard deviations.

| | 5 | 24 | 29 | 1 | 15 | 286 |
|---|---|---|---|---|---|---|
| Si–O–Al | 147.26(4.04) | 147.46(5.48) | 147.62(3.08) | 146.55(4.85) | 147.12(3.06) | 148.75(7.36) |
| O–Si–O | 109.48(3.78) | 109.48(3.54) | 109.49(3.99) | 109.48(3.64) | 109.48(3.61) | 109.48(3.96) |
| O–Al–O | 109.43(3.92) | 109.43(3.91) | 109.45(3.75) | 109.42(3.71) | 109.42(4.15) | 109.43(3.89) |
| Si–O (Å) | 1.629(0.014) | 1.629(0.013) | 1.629(0.013) | 1.629(0.014) | 1.629(0.013) | 1.629(0.010) |
| Al–O (Å) | 1.748(0.017) | 1.749(0.015) | 1.748(0.018) | 1.750(0.018) | 1.749(0.014) | 1.748(0.020) |
| Na–O (Å)(1) | 2.327(0.019) | 2.323(0.016) | 2.338(0.028) | 2.310(0.026) | 2.327(0.004) | 2.61(0.33) |
| Na–O (Å)(2) | 2.911(0.088) | 2.894(0.127) | 2.903(0.085) | 2.930(0.097) | 2.907(0.057) | |
| Na–Na (Å) | 4.620(0.056) | 4.663(0.083) | 4.642(0.025) | 4.587(0.060) | 4.603(0.010) | 4.734(0.157) |
| O–O (Si) (Å) | 2.658(0.059) | 2.659(0.055) | 2.659(0.063) | 2.660(0.057) | 2.659(0.055) | 2.659(0.064) |
| O–O (Al)(Å) | 2.853(0.063) | 2.853(0.063) | 2.852(0.061) | 2.855(0.057) | 2.853(0.067) | 2.853(0.067) |
| $\phi$ (Si) | 15.48(2.03) | 15.36(2.50) | 15.04(2.001) | 16.39(1.73) | 15.61(1.88) | 13.13(4.85) |
| $\phi$ (Al) | 14.55(1.88) | 14.45(2.33) | 14.14(1.86) | 15.42(2.07) | 14.67(1.69) | 12.34(4.34) |

local distortions from neighboring vacancies occur cooperatively. In a configuration like #29 however, certain pairs of vacancies are in 6-rings that share a T-atom. For these rings to distort so as to reduce the Coulomb repulsion energy would require at least two of the six O–T–O angles to deviate significantly from 109.47°. This is much more costly than varying the Al–O–Si angle and so the framework cannot stabilize the vacancy sublattice as effectively.

The extent to which the framework of given cation-vacancy configuration distorts from the initial cubic structure can be quantified by calculating the mean-square displacements of the T-atoms from their equivalent sites in the undistorted cubic lattice. Table IX shows these displacements for the five configurations that have all vacancies on (110) planes. Notice that #24 undergoes the largest deviation while #29 undergoes the smallest. Except for configuration #15, the values in Table IX appear to correlate with the structural energy. The problem with #15, despite the advantage of fully-separated vacant windows, is its high symmetry—all vacancies lie in chains parallel to a threefold symmetry axis of the framework. The lower number of internal degrees of freedom places additional limits on the nature of the framework response that #15 can undergo.

While it is not possible to rationalize the energies of these five structures in terms of $Na^+$–$Na^+$ Coulomb repulsion energy or framework relaxation alone, the interplay of these two influences are sufficient. Configurations #24 and #15 both possess the unique advantage of fully separated vacant 6-ring windows, which brings them both to the low-energy end of the spectrum. Configuration #15 possesses the minimum-energy vacancy arrangement in the unrelaxed structure; but configuration #24 has a much lower symmetry, with more internal degrees of freedom that can respond to its vacancy ordering. Configuration #24 achieves both a more effective framework response *and* greater Na–Na separation. This tips the scales in favor of the lower-symmetry superstructure of configuration #24.

Configuration #286 has a summed mean-square displacement of 2.42, much larger than the structures in Table IX. As already stated, this configuration is unusual in having two very distinct cage types—one with no vacant windows and one with four vacant windows. In the former case it would be favorable for the cage to undergo a large structural collapse, as in NaCl–SOD, while in the latter it would prefer to expand. This results in the large mean-squared displacement and the very large deviations in the average structural parameters, as evident in Table VIII. Note in particular the large standard deviations in the Si–O–Al bond angle and in the collapsing angles. The Na–O bond distances cannot readily be broken down into two groups, so only one average is given. On average #286 has the largest Na–Na distance upon minimization, but once again the standard deviation is very large—some pairs are less than 4.5 Å apart, thus raising the Coulombic repulsion energy. This fact, and the large

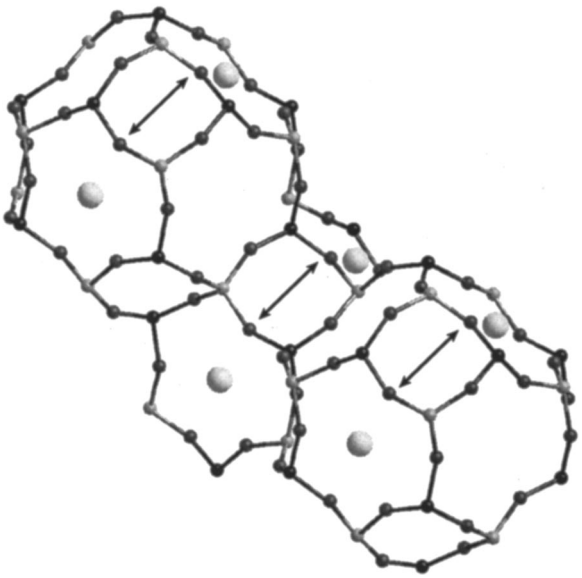

FIG. 8. A section of the full configuration #24 structure. The light spheres correspond to vacant 6-ring windows. The arrows show how the Si–O–Al bond angles of the 4-rings participate in the distortion driven by the vacancy ordering.

TABLE IX. Summed mean-square displacements of the T-atoms of the 84-atom supercell from their initial high-symmetry positions in the original cubic lattice.

| | 5 | 24 | 29 | 1 | 15 |
|---|---|---|---|---|---|
| $\sigma^2$ (Å$^2$) | 0.73 | 0.84 | 0.26 | 0.32 | 0.32 |

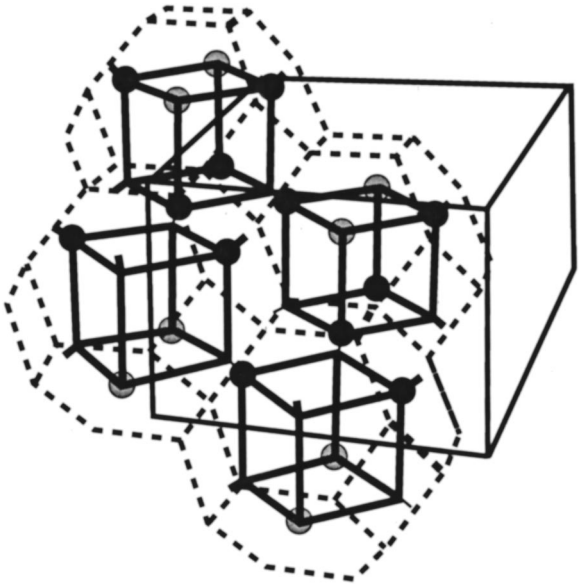

FIG. 9. The off-window Na cation positions in configuration #24. The unit cell is shown as a solid line, while the sodalite cages are shown as dashed lines. The small solid-lined cubes, corresponding to the four cages per unit cell, connect the eight window positions within each cage. The cube corners that face occupied windows are also decorated with short lines, indicating that the corresponding cation is on one side of the window or the other, but not both. The 12 filled circles are the nonvacant Na sites. The shaded circles indicate vacant windows—one is drawn on each side of the vacant window, hence eight appear in the diagram, though there are only four vacant 6-ring windows per unit cell.

framework distortion needed to accommodate the unusual Na cation ordering, raises the structural energy of #286 above #24, #15, and #5, although it is remarkable that its energy is lower than #29 and #1 considering its very high unrelaxed Na–Na repulsive energy.

### B. Off-window $Na^+$ cation shifts in configuration #24

One issue that has been ignored in the discussion thus far is the shift of the Na cations off from the centers of their 6-ring windows upon relaxation. Though these shifts are not large (0–0.35 Å), they are nevertheless significant, and effectively identify a given cation with the cage into which it shifts. One might anticipate that the lowest-energy structure would have 3 Na cations per cage, as is the case with the type-I and type-III structures, where it turns out that the Na cations arrange themselves in each cage like the three corners of a tetrahedron missing one vertex. Recall that the original 42-atom unit cell contains two sodalite cage volumes related by body centering. With type-I, the missing vertex is oriented the same way in every cage, whereas the two cages of the type-III unit cell contain differently oriented missing vacancies. The type-II system is altogether different; one of the two cages contains a complete tetrahedron of four Na cations, while the other cage gets only two cations. And because configuration #24 consists of an arrangement type-II cages in the supercell setting, two of its cages contain complete Na tetrahedra, while the other two cages contain only two Na cations each. The resulting cation/vacancy configuration, shown schematically in Fig. 9, is characterized in the supercell setting by alternating $x'z'$ planes of four-cation cages and two-cation cages.

TABLE X. Atomic coordinates for $Na_6$–SOD using the configuration #24 model in the supercell setting.

| Atom | X | Y | Z |
|---|---|---|---|
| Si | 0.126 | 0.874 | 0.999 |
| Si | 0.380 | 0.628 | 0.003 |
| Si | 0.757 | 0.748 | 0.248 |
| Al | 0.247 | 0.748 | 0.250 |
| Al | 0.873 | 0.876 | 0.992 |
| Al | 0.624 | 0.625 | 0.006 |
| O | 0.639 | 0.503 | 0.962 |
| O | 0.340 | 0.693 | 0.848 |
| O | 0.300 | 0.656 | 0.153 |
| O | 0.506 | 0.858 | 0.516 |
| O | 0.656 | 0.690 | 0.863 |
| O | 0.700 | 0.647 | 0.147 |
| O | 0.301 | 0.842 | 0.652 |
| O | 0.693 | 0.845 | 0.637 |
| O | 0.341 | 0.800 | 0.345 |
| O | 0.658 | 0.809 | 0.347 |
| O | 0.507 | 0.653 | 0.058 |
| O | 0.159 | 0.003 | 0.957 |
| Na | 0.501 | 0.740 | 0.275 |
| Na | 0.738 | 0.999 | 0.229 |
| Na | 0.222 | 0.503 | 0.237 |

Table X includes a full list (space-group $Pnc2$) of atomic coordinates obtained from the GGA DFT minimization of configuration #24. Because the calculations were performed assuming only P1 symmetry, the resulting structure was then analyzed using the FindSymmetry feature of InsightII software suite from Molecular Simulations Inc. (MSI), which determined the space-group symmetry and subsequently symmetrized the coordinates. From these coordinates, the off-window Na shifts are found to range between 0.25 Å and 0.35 Å.

## V. CONCLUSIONS

The calculations and analyses implemented here complement previous experimental x-ray powder diffraction studies, making it possible to unambiguously determine the low-temperature cation-ordered structure of anhydrous $Na_6$–SOD. Due to the unavailability of single crystal samples, the complexity of experimental PXD data, and the large number of possible vacancy orderings, this structure has resisted determination for several years. By providing the additional insight offered by computer modeling, a unique solution has now been identified that minimizes the structural energy and best matches experimental observations. Constrained by the experimentally observed supercell, each possible cation-vacancy ordering has been investigated via a variety of theoretical methods and computational tools. Initially, the $Na^+$–$Na^+$ Coulomb repulsion energy of the unrelaxed cation-vacancy orderings was used as an indicator of stability. More refined indicators were then found in full lattice-energy minimizations of both structure and unit cell parameters using both the BWM and shell-model potentials with the GULP software package. Irrespective of the force-field used, a family of five closely related cation-vacancy

orderings was found to be most energetically favorable, which were then further examined by more powerful *ab initio* GGA DFT calculations. The lowest-energy configuration (#24) proved to drive the formation of a volume-doubled pseudo-tetragonal supercell and yield calculated superlattice peak intensities that qualitatively match recent experimental observations. A number of factors contribute to the low-energy of this structure. The avoidance of nearest-neighbor vacant 6-ring windows ensures an even distribution of cation charge throughout the structure. The avoidance of vacant-window pairs that share a common vertex (Si or Al atom) allow the vacant windows to expand cooperatively rather than competitively. This degree of cooperativity is maximized when the framework distortion propagates along one of the translational axes of the cell. This can only occur when the 4 rings in the $x-y$ plane have their sides parallel to the translational axes of the solid. This is why the translational symmetry axes are $x'=(x+y)$ and $y'=(x-y)$ and not $x$ and $y$. It also explains why the resulting cell is based on a tetragonal supercell (we have verified this by looking at all vacancies distributions in cells based on a $2a\times a\times a$ arrangement of cages and found them to be higher in energy). Finally, relatively low space-group symmetry provides many internal degrees of freedom through which to relieve the stresses induced by the vacant windows and minimize the Coulomb repulsion energy of the Na ion distribution.

## ACKNOWLEDGMENTS

This work was funded by the Office of Naval Research, NSF CHE 97-09038, and by the MRL Program of the National Science Foundation under Award No. DMR96-32716. Computational facilities were provided in part by NSF Grant No. CDA96-01954 and by Silicon Graphics Inc. We would like to also thank Dr. Julian Gale (Imperial College, London), who kindly allowed us to use his General Utility Lattice Program (GULP).

[1] L. Pauling, Z. Kristallogr. **74**, 213 (1930).
[2] I. Hassan and H. D. Grundy, Acta Crystallogr., Sect. B: Struct. Sci. **B40**, 6–13 (1984).
[3] S. E. Latturner, J. Sachleben, B. B. Iversen, J. Hanson, and G. D. Stucky, J. Phys. Chem. B **103**, 7135 (1999).
[4] J. Felsche, S. Luger, and C. Baerlocher, Zeolites **6**, 367 (1986).
[5] P. Sieger, Ph.D. thesis, University Constance, Germany, 1992.
[6] B. J. Campbell, J. M. Delgado, A. K. Cheetham, B. B. Iverson, N. P. Blake, S. R. Shannon, S. Latturner, and G. D. Stucky, J. Chem. Phys. **113**, 10226 (2000), following paper.
[7] P. Behrens, P. B. Kempa, S. Assmann, M. Wiebcke, and J. Felsche, J. Solid State Chem. **115**, 55 (1995).
[8] A. M. Rappe, K. M. Rabe, E. Kaxiras, and J. D. Joannopoulos, Phys. Rev. B **41**, 1227 (1990).
[9] J. P. Perdew and Y. Wang, Phys. Rev. B **44**, 13298 (1991).
[10] G. Kresse and J. Hafner, Phys. Rev. B **48**, 13115 (1993).
[11] G. Kresse and J. Furthmuller, Phys. Rev. B **54**, 11169 (1996).
[12] N. P. Blake, P. C. Weakliem, and H. Metiu, J. Phys. Chem. B **102**, 67 (1998).
[13] J. D. Gale, J. Chem. Soc., Faraday Trans. **93**, 629 (1997).
[14] B. G. Dick, Jr. and A. W. Overhauser, Phys. Rev. **112**, 90 (1958).
[15] M. J. Sanders, M. Leslie, and C. R. A. Catlow, J. Chem. Soc. Chem. Commun. **1984**, 1271.
[16] R. A. Jackson and C. R. A. Catlow, Mol. Simul. **1**, 207 (1988).
[17] K. T. Thomson, R. M. Wentzcovitch, A. McCormick, and H. T. Davis, Chem. Phys. Lett. **283**, 39 (1998).
[18] F. Fillopone, F. Buda, S. Iarlori, G. Moretti, and P. Porta, J. Phys. Chem. **99**, 12883 (1995).